Research Article

Check for updates

Performance assessment of pantograph and overhead system based on a vertical coupling dynamics model of the railway system

Yang Song[1], Fuchuan Duan[2]

[1]Department of Structural Engineering, Norwegian University of Science and Technology, Trondheim 7034, Norway.
[2]Institute of Rail Transit, Tongji University, Shanghai 201804, China.

Correspondence to: Dr. Yang Song, Department of Structural Engineering, Norwegian University of Science and Technology, Richard Birkelands vei 1A, Trondheim 7034, Norway. E-mail: y.song_ac@hotmail.com

Abstract

The increase of train speed leads to a violent vibration of the pantograph and overhead system. To evaluate the interaction performance of the pantograph and overhead system, a whole railway dynamics model including the track, vehicle, pantograph, and overhead system is established. The overhead system is represented by the finite element approach using the analytical formulas of nonlinear cable and truss elements. The vehicle is modeled by a multi-rigid-body system with a pantograph installed on its roof. A beam element with elastic foundations is used to model the track, which possesses harmonic and random irregularities. An iterative algorithm is implemented to solve the nonlinear behavior of the coupling model. The nonlinearities in the deformation of overhead system, the contact of the pantograph and contact line, and the contact of the vehicle-track are properly considered. Several numerical simulations are implemented to systematically investigate the influence of the vehicle-track vibration on the dynamic behavior of pantograph and overhead system. The results indicate that the vehicle-track vibration induced by the rail irregularities with large amplitude or certain wavelength can significantly aggravate the interaction performance of pantograph and overhead system.

Keywords: Railway, overhead system, coupling dynamics, nonlinearity, finite element, rail irregularity

1. INTRODUCTION

The pantograph and overhead system play an important role in modern high-speed railway systems, as they are responsible for the continuous transmission of electric energy from the power supply to the locomotive. The current collection quality of high-speed trains is directly determined by the mechanical interaction performance between the panhead of the pantograph and the contact line of the overhead system. With the rapid expansion of the high-speed rail industry, the increase of train speed leads to a more violent vibration of the pantograph and overhead system, which directly results in many issues in current collection quality. For instance, the contact loss leads to arcing and power supply interruption, and the contact force results in excessive wear of the contact surface. The pantograph and overhead system have been recognized as the most vulnerable parts in the traction power system, as they suffer a number of disturbances, such as the vehicle-track perturbations[1,2], material stress in wires[3,4], anomalies of the overhead system[5,6], temperature variance[7], and environmental perturbations[8,9].

Due to the tremendous cost of field tests, mathematic modeling is an effective method to describe the complex dynamic behavior of pantograph and overhead system. Zhang *et al.* reviewed various kinds of mathematic models of pantograph and overhead system from a general perspective of railway dynamics[10]. Liu *et al.* gave an overview of the advances in research on the modeling of high-speed railway overhead system[11]. Some particular methods have been proposed to efficiently evaluate the dynamic interaction performance of pantograph and overhead system. The following examples are the particular ones that deserve to be mentioned. Song *et al.* proposed a nonlinear cable-based model for the overhead system, in which the nonsmooth nonlinearity of droppers and geometrical nonlinearity of wires can be fully considered[12]. Yao *et al.* included the effect of ice in the overhead system model with different approaches and compared their advantages[13]. Tur *et al.* proposed a 3D absolute nodal coordinate finite element model to compute the initial configuration of a railway overhead system[14]. Bautista *et al.* proposed a combination method to implement the simulation of the interaction behavior of a multibody pantograph model and a finite element model of overhead system[15]. To improve the interaction performance, several effective measures, such as the active control of pantograph[16], optimization of structure[17], and damper designed for pantograph[18], are developed. To master the health condition of the overhead system, several monitoring techniques[19–21] and performance assessment methods[22,23] are developed to capture the dynamic response and static geometry of the overhead system.

From the above literature review, it can be seen that the dynamic behavior of pantograph and overhead system is mostly studied without considering vehicle-track perturbations. The interaction of pantograph and overhead system can be recognized as a vertical contact. The vertical vibration of the vehicle may have some noticeable effect on the contact of the pantograph and the overhead system. In[24], a spatial model of pantograph-catenary-vehicle-track system is established to investigate the dynamic performance of pantograph-catenary with random perturbations of vehicle-track. The main finding indicates that the vertical vibration of the car body has the most noticeable effect on the pantograph-catenary interaction. Thus, the main purpose of the present paper is to establish a more detailed model for the vertical railway dynamic systems, including the overhead system, pantograph, vehicle, and track. For the overhead system, a nonlinear finite element approach is employed based on the analytical formulas of nonlinear cable and truss elements. The vehicle is represented as a multi-rigid-body model with a pantograph installed on its roof. The rail is modeled as an Euler-Bernoulli beam supported by elastic foundations comprised of ballasts and sleepers. The contact between the track and wheel is characterized by the well-known Hertzian contact theory, and the contact between the pantograph and the contact line is implemented by a penalty method. The analysis of the influence of the vehicle-track vibration mainly focuses on two aspects. The first one is the influence of rail irregularity with a specific wavelength and wave depth on the interaction performance of pantograph and overhead system. The second one focuses on the influence of random rail irregularities. Furthermore, the influence of the vibration induced by the high-speed vehicle and the modern ballastless track on the pantograph and overhead system interaction
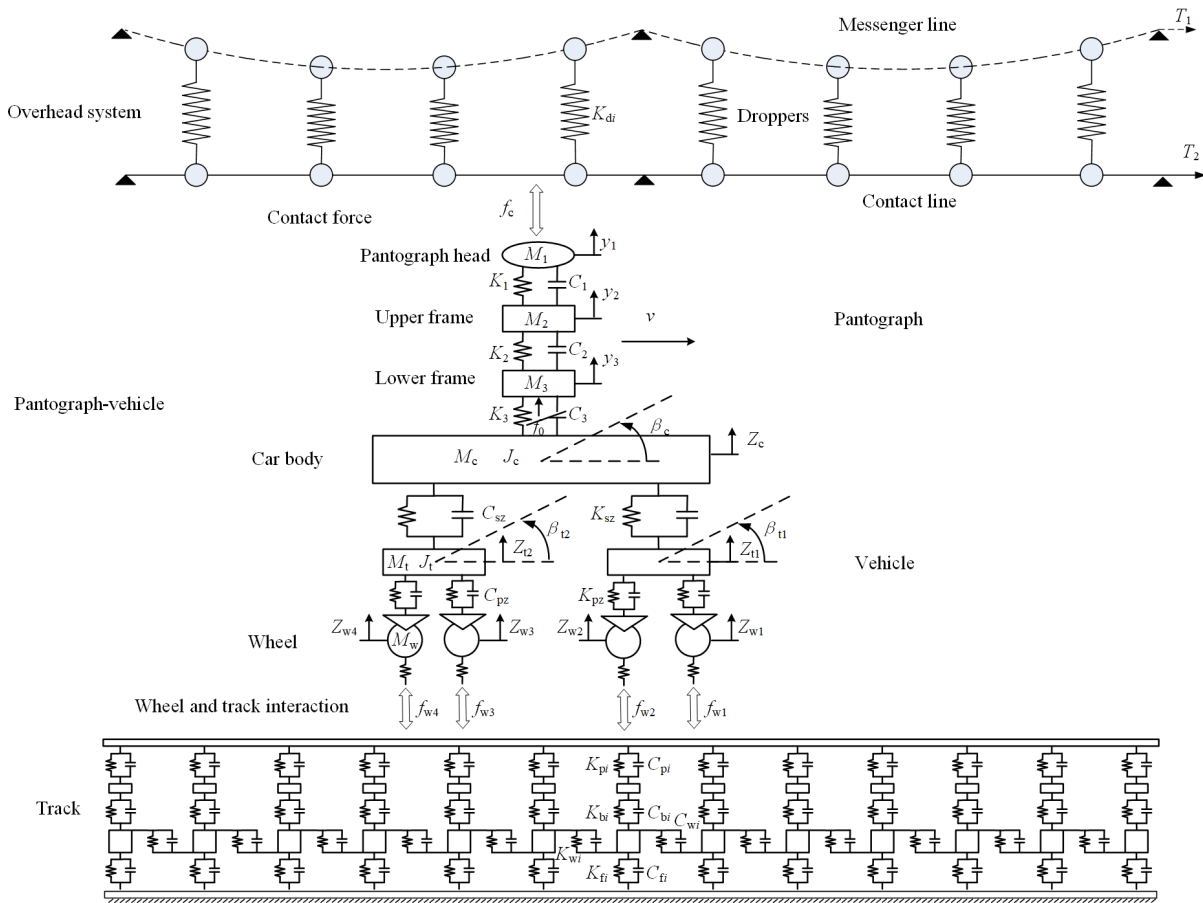
Figure 1. Vertical coupling model for overhead system-pantograph-vehicle-track system.

is studied and compared with the traditional track. The influence of the parameters of the lower frame of the pantograph which connects with the car body roof is also investigated.

2. VERTICAL COUPLING MODEL FOR RAILWAY SYSTEM

Figure 1 presents the whole coupling model for the railway system, which is mainly comprised of three subsystems: overhead system, pantograph-vehicle, and track. Obviously, there is a dynamic interaction between the overhead system and pantograph and between the vehicle and the track through the contact forces f_c and $f_{w1} - f_{w4}$, respectively. In this section, the modeling methods of these three subsystems are presented.

2.1. Modeling of overhead system

The overhead system is comprised of three main components. The contact line is responsible for providing the electrical energy through a pantograph to the high-speed train. In this paper, the finite element method widely used to address complex engineering systems[25–28] is adopted here to model the overhead system. The messenger line and droppers are used to support the contact line. The contact and messenger lines are discretized as a number of nonlinear cable elements according to the concept of the finite element method. Figure 2 presents a segment of the nonlinear cable with an unstrained length of l_0. The relationship between
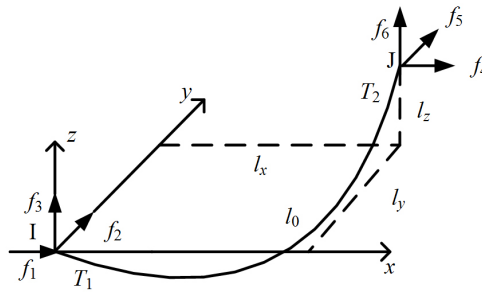
Figure 2. Nonlinear cable element.

the relative positions l_x, l_y, and l_z of the two nodes and the nodal forces $f_1 \sim f_6$ is governed by Equation (1) [12].

$$l_x = -\frac{f_1 l_0}{EA} - \frac{f_1}{w}\left\{\ln\left(\sqrt{f_4^2 + f_5^2 + f_6^2} + f_6\right) - \right.$$
$$\left.\ln\left(\sqrt{f_1^2 + f_2^2 + f_3^2} - f_3\right)\right\}$$

$$l_y = -\frac{f_2 l_0}{EA} + \frac{f_2}{w}\left\{\ln\left[\sqrt{f_1^2 + f_2^2 + (wl_0 - f_3)^2}\right.\right.$$
$$\left.+ wl_0 - f_3\right] - \ln\left(\sqrt{f_1^2 + f_2^2 + f_3^2} - f_3\right)\right\}$$

$$l_z = -\frac{f_3 l_0}{EA} + \frac{wl_0^2}{2EA} +$$
$$\frac{1}{w}\left[\sqrt{f_4^2 + f_5^2 + f_6^2} - \sqrt{f_1^2 + f_2^2 + f_3^2}\right]$$

(1)

in which w is the self-weight. E and A denote the Young's modulus and the cross-sectional area of the messenger/contact wire, respectively. The relationship between the nodal forces $f_1 \sim f_3$ at node I and $f_4 \sim f_6$ at node J can be expressed as

$$f_4 = -f_1 \quad f_5 = -f_2 \quad f_6 = -f_3 + wl_0 \tag{2}$$

By differentiating both sides of Equation (1), the flexibility stiffness can be obtained.

$$\begin{Bmatrix} dl_x \\ dl_y \\ dl_z \end{Bmatrix} = \begin{bmatrix} \dfrac{\partial l_x}{\partial f_1} & \dfrac{\partial l_x}{\partial f_2} & \dfrac{\partial l_x}{\partial f_3} \\ \dfrac{\partial l_y}{\partial f_1} & \dfrac{\partial l_y}{\partial f_2} & \dfrac{\partial l_y}{\partial f_3} \\ \dfrac{\partial l_z}{\partial f_1} & \dfrac{\partial l_z}{\partial f_2} & \dfrac{\partial l_z}{\partial f_3} \end{bmatrix} \begin{Bmatrix} df_1 \\ df_2 \\ df_3 \end{Bmatrix} + \begin{Bmatrix} \dfrac{\partial l_x}{\partial L_0} \\ \dfrac{\partial l_y}{\partial L_0} \\ \dfrac{\partial l_z}{\partial L_0} \end{Bmatrix} dl_0$$
$$= \mathbf{G}_C^e d\mathbf{F}^e + \mathbf{G}_G^e dL_0$$

(3)

where dl_x, dl_y, and dl_z are the increments of the relative positions in x, y, and z directions, respectively. df_1, df_2, and df_3 represent the increments of the corresponding internal force. The stiffness matrix can be obtained by inverting flexibility matrices $\mathbf{G}_C^e$, which is updated in each iterative step according to the nodal forces $f_1 \sim f_6$ to ensure accuracy when large deformation of the messenger/contact wire occurs. The vector $\mathbf{G}_G^e$ related to dl_0 is used to solve the initial state. Equation (3) can be rewritten as

$$d\mathbf{F}^e = \mathbf{K}_C^e d\mathbf{X}^e + \mathbf{K}_G^e dl_0 \tag{4}$$

where

$$\mathbf{dF}^{e} = \begin{Bmatrix} df_1 \\ df_2 \\ df_3 \\ df_4 \\ df_5 \\ df_6 \end{Bmatrix} \quad \mathbf{dX}^{e} = \begin{Bmatrix} dx_1 \\ dy_1 \\ dz_1 \\ dx_2 \\ dy_2 \\ dz_2 \end{Bmatrix} \quad \mathbf{K}_{C}^{e} = \begin{bmatrix} -\mathbf{K}_{F}^{e} & \mathbf{K}_{F}^{e} \\ \mathbf{K}_{F}^{e} & -\mathbf{K}_{F}^{e} \end{bmatrix} \tag{5}$$

$$\mathbf{K}_{G}^{e} = \begin{bmatrix} -\mathbf{K}_{F}^{e}\mathbf{G}_{G}^{e} \\ \begin{bmatrix} 0 & 0 & w \end{bmatrix}^{\mathbf{T}} + \mathbf{K}_{F}^{e}\mathbf{G}_{G}^{e} \end{bmatrix} \quad \mathbf{K}_{F}^{e} = \begin{bmatrix} \mathbf{G}_{C}^{e} \end{bmatrix}^{-1}$$

It is worth noting that, after the initial configuration is determined, the initial length l_0 of the cable does not change. Thus, Equation (4) is written as the following equation with a constant initial length l_0 in the dynamic simulation.

$$\mathbf{dF}^{e} = \mathbf{K}_{C}^{e}\mathbf{dX}^{e} \tag{6}$$

Droppers only can work in tension and have no resistance to compression force, which behave as one-sided trusses. In this paper, a similar approach is adopted to derive the stiffness matrix of a truss element. Then, a shape-finding method is adopted to calculate the initial configuration of the overhead system, which has been verified by several numerical examples[29]. After the initial configuration is determined, a nonlinear finite element dynamic analysis is performed to solve the dynamic response of the overhead system. The global stiffness matrix $\mathbf{K}_{C}(t)$ of the overhead system can be formulated through the finite element approach at time instant t. In combination with the global lumped mass matrix $\mathbf{M}_{C}$ and the global damping matrix $\mathbf{C}_{C}$, the equation of motion can be written as

$$\mathbf{M}_{C}\Delta\ddot{\mathbf{X}}_{C}(t) + \mathbf{C}_{C}\Delta\dot{\mathbf{X}}_{C}(t) + \mathbf{K}_{C}(t)\Delta\mathbf{X}_{C}(t) = \Delta\mathbf{F}_{C}(x,t) \tag{7}$$

where $\Delta\ddot{\mathbf{X}}_{C}(t)$, $\Delta\dot{\mathbf{X}}_{C}(t)$, and $\Delta\mathbf{X}_{C}(t)$ are the incremental vectors of the global acceleration, velocity, and displacement for the overhead system, respectively. $\Delta\mathbf{F}_{C}(x,t)$ on the right side is the incremental vector of the excitation, which includes the contact force exerted on the contact point and the internal force of the structure. It is noted that the stiffness matrix $\mathbf{K}_{C}(t)$ updates in each time step according to the deformation of contact/messenger wires and droppers to take the geometrical nonlinearity and dropper slackness into account.

2.2. Modeling of pantograph-vehicle

As shown in Figure 1, the pantograph-vehicle is modeled as a multi-rigid-body system with 13 DOFs (degrees of freedom). Apart from the vertical motion, the rolling motions of the car body β_c and bogies $\beta_{t1} \sim \beta_{t2}$ are also considered. The equation of motion for the pantograph-vehicle system can be obtained as[30]

$$\mathbf{M}_{V}\ddot{\mathbf{X}}_{V}(t) + \mathbf{C}_{V}\dot{\mathbf{X}}_{V}(t) + \mathbf{K}_{V}\mathbf{X}_{V}(t) = \mathbf{F}_{V}(t) \tag{8}$$

where $\mathbf{M}_{V}$, $\mathbf{C}_{V}$, and $\mathbf{K}_{V}$ are the mass, damping, and stiffness matrices for the pantograph-vehicle system, respectively. $\ddot{\mathbf{X}}_{V}(t)$, $\dot{\mathbf{X}}_{V}(t)$, and $\mathbf{X}_{V}(t)$ are the corresponding global acceleration, velocity, and displacement vectors. $\mathbf{F}_{V}(t)$ is the external force vector, which can be expressed as

$$\mathbf{F}_{V}(t) = \{ - f_c \, 0 \, f_0 - M_c g \, 0 - M_t g \, 0 - M_t g \, 0 - M_{wi} g + 2 f_{w1}$$
$$- M_{w2} g + 2 f_{w2} - M_{w3} g + 2 f_{w3} - M_{w4} g + 2 f_{w4} \}^{\mathrm{T}} \tag{9}$$

where f_0 is the static lift force exerted on the lower frame of pantograph. M_c, M_t, and M_{wi} are the masses of the car body, bogie, and wheel, respectively.

2.3. Modeling of track

The railway track is modeled by the Euler-Bernoulli beam supported by elastic foundations, comprised of the sleepers and ballasts. The equation of motion for the rail can be written as

$$EI_r \frac{\partial^4 w_r}{\partial x^4}(x,t) + \rho_r \frac{\partial^2 w_r}{\partial t^2}(x,t) = \sum_{i=1}^{n_r} f_{ri} \delta\left(x - x_r^i\right) + \sum_{j=1}^{4} f_{wj} \delta\left(x - x_{wj}\right) \tag{10}$$

where EI_r is the flexural rigidity of rail. ρ_r is the density per length. f_{ri} and x_r^i are the external force and the position of the ith elastic supporter. n_r is the number of the elastic foundations. x_{wj} is the contact point between the jth wheel and the rail. This partial differential equation can be solved through the modal superposition method or the finite element method. Here, the former is adopted. The analytical solution of Equation (10) can be written as [31]

$$w_r(x,t) = \sum_{u=1}^{\infty} \psi_u(x) q_u(t) \tag{11}$$

where $q_u(t)$ is the $u-$order generalized displacement. $\psi_u(x)$ is the corresponding modal function. By substituting Equation (16) into Equation (15), the equation of motion for rail can be rewritten as

$$\ddot{q}_u(t) + \frac{EI_r}{\rho_r}\left(\frac{u\pi}{l}\right)^4 q_u(t) = -\sum_{i=1}^{n_r} f_{ri}(t) \psi_u(x_i) + \sum_{j=1}^{4} f_{wj}(t) \psi_u(x_{wj}) \tag{12}$$

where $f_{ri}(t)$ can be obtained as

$$f_{ri}(t) = C_{pi} \frac{\partial w_r}{\partial t}(x_i,t) + K_{pi} w_r(x_i,t) - C_{pi} \frac{\partial Z_{si}(t)}{\partial t} - K_{pi} Z_{si}(t) \qquad (i = 1 \sim n_r) \tag{13}$$

with C_{pi} and K_{pi} the damping and stiffness of the ith sleeper, respectively. $Z_{si}(t)$ is the vertical displacement of the ith sleeper, which is determined by the equation of motion for sleeper.

$$K_{pi}\left[w_r(x_i,t) - Z_{si}(t)\right] + C_{pi}\left[\frac{\partial w_r(x_i,t)}{\partial t} - \frac{dZ_{si}(t)}{dt}\right]$$
$$- K_{bi}\left[Z_{si}(t) - Z_{bi}(t)\right] - C_{bi}\left[\frac{dZ_{si}(t)}{dt} - \frac{dZ_{bi}(t)}{dt}\right] = M_{si}\frac{d^2 Z_{si}(t)}{dt^2} \qquad (i = 1 \sim n_r) \tag{14}$$

where M_{si} is the mass of the ith sleeper. C_{bi} and K_{bi} are the damping and stiffness of the ith ballast. $Z_{bi}(t)$ is the corresponding vertical displacement of the ith ballast, which is governed by the following equation:

$$M_{bi}\frac{d^2 Z_{bi}(t)}{dt^2} + (C_{bi} + C_{fi} + 2C_{wi})\frac{dZ_{bi}(t)}{dt} + (K_{bi} + K_{fi} + 2K_{wi}) Z_{bi}(t)$$
$$- C_{bi}\frac{dZ_{si}(t)}{dt} - K_{bi}Z_{si}(t) - C_{wi}\frac{dZ_{b(i+1)}(t)}{dt} - K_{wi}Z_{b(i+1)}(t) - C_{wi}\frac{dZ_{b(i-1)}(t)}{dt} \tag{15}$$
$$- K_{wi}Z_{b(i-1)}(t) = 0 \qquad (i = 1 \sim n_r)$$

C_{wi} and K_{wi} are the damping and stiffness of the ith subgrade, respectively. The boundary conditions are defined as

$$\begin{cases} Z_{b0}(t) = \dfrac{dZ_{b0}(t)}{dt} = 0 \\ Z_{b(n_r+1)}(t) = \dfrac{dZ_{b(n_r+1)}(t)}{dt} = 0 \end{cases} \tag{16}$$

By substituting Equations (11)-(16) into Equation (10), the equation of motion for track can be obtained as

$$\mathbf{M}_T\ddot{\mathbf{X}}_T(t) + \mathbf{C}_T\dot{\mathbf{X}}_T(t) + \mathbf{K}_T\mathbf{X}_T(t) = \mathbf{F}_T(t) \tag{17}$$

where $\mathbf{M}_T$, $\mathbf{C}_T$, and $\mathbf{K}_T$ are the mass, damping, and stiffness matrices, respectively. $\ddot{\mathbf{X}}_T(t)$, $\dot{\mathbf{X}}_T(t)$, and $\mathbf{X}_T(t)$ are the generalized global acceleration, velocity, and displacement vectors, respectively. The vertical deflection of rail can be calculated according to Equation (11). $\mathbf{F}_T(t)$ is the generalized external excitation.

2.4. Contact model

The sliding contact between the pantograph and the contact line is implemented by the penalty method, in which the contact is defined through an assumption of a contact stiffness. The contact force is calculated based on a penalization of the interpenetration between the pantograph head and the contact line. The contact force is expressed as [32,33]

$$f_c = \begin{cases} K_S(y_1 - y_c) & y_1 \geq y_c \\ 0 & y_1 < y_c \end{cases} \tag{18}$$

where K_S is the contact stiffness. y_1 is the vertical displacement of the pantograph head. y_c is the vertical displacement of the contact line at the contact point. In this work, a large contact stiffness of 200,000 N/m is adopted in the numerical simulation to ensure that the response at the frequency range of interest cannot be contaminated.

The contact interface between the vehicle and track is between the wheel and the rail, which exhibits significant nonlinearity. The nonlinear contact can be described by Hertzian nonlinear theory of elasticity. The wheel-rail contact force can be calculated through the following equation [34]:

$$f_{wj}(t) = \begin{cases} \left\{ \dfrac{1}{G}\left[w_r(x_{wj}, t) - Z_{wj} - w_0(t)\right] \right\}^{1.5} & w_r(x_{wj}, t) - Z_{wj} - w_0(t) \geq 0 \\ 0 & w_r(x_{wj}, t) - Z_{wj} - w_0(t) < 0 \end{cases} \tag{19}$$

where G is the contact constant. Due to the use of the nonlinear Hertzian nonlinear contact model, the kinetic equations of the vehicle and the track should be calculated separately. The solution procedure for coupling the pantograph-overhead system and vehicle-track is discussed in the next section. The selection of parameter G refers to the method in [34].

2.5. Verification of the model

It is difficult to find measurement data or a proper standard to validate the whole coupling dynamics model. The whole model is divided into the pantograph-overhead system model and the vehicle-track model. The validation of each model is made independently. In [12], the pantograph-overhead system model is verified through a series of numerical examples. Here, the parameters of pantograph and overhead system in EN 50318 [35] are adopted to undertake the simulation using the presented model. The statistics of the simulation results are listed in Table 1 according to EN 50318. It can be found that the simulation results show excellent

Table 1. Validation of the pantograph and overhead system mode according to EN 50318

Speed	275 [km/h]			
Pantograph	1		2	
	Range of acceptance	Result	Range of acceptance	Result
F_m [N]	141.5-146.5	143.1	141.5-146.5	144.4
δ [N]	31.9-34.8	33.3	50.0-54.5	51.6
δ (0-5 Hz) [N]	26.4-28.9	27.2	41.2-45.4	42.8
δ (5-20 Hz) [N]	16.2-22.4	19.3	25.2-34.7	29.3
F_{max} [N]	211.9-244	222.9	241-290	260.4
F_{min} [N]	71-86	85.8	14-50	34.5
Speed	320 [km/h]			
Pantograph	1		2	
	Range of acceptance	Result	Range of acceptance	Result
F_m [N]	166.5-171.5	169.4	166.5-171.5	168.8
δ [N]	49.5-62.9	53.7	30.2-43.8	42.3
δ (0-5 Hz) [N]	38.7-44.4	40.1	14.3-23.3	19.0
δ (5-20 Hz) [N]	29.0-46.2	35.7	29.0-46.2	37.9
F_{max} [N]	295-343	295.0	252-317	269.5
F_{min} [N]	55-82	60.0	51-86	59.7

Table 2. Parameters of the high-speed vehicle

Car body mass (kg)	52000
Car body pitch moment of inertia (kg m^2)	2.31×10^6
Bogie mass (kg)	3200
Bogie pitch moment of inertia (kg m^2)	3120
Wheelset mass (kg)	1400
Primary suspension stiffness (N/m)	1.87×10^6
Primary suspension damping (N s/m)	5×10^5
Secondary suspension stiffness (N/m)	1.72×10^6
Secondary suspension damping (N s/m)	1.96×10^5
Distance between two bogie centers (m)	18
Distance between two axles of the same bogie (m)	2.5
Wheel rolling radius (m)	0.4575

agreements with the requirements of EN 50318. Thus, the pantograph and overhead system model are thought to be valid.

For the validation of the vehicle-track model, the high-speed vehicle-track parameters listed in Table 2 and Table 3 are adopted [34]. The simulation results are compared with the results of the Zhai model, which is a simulation method for the vertical interactions between cars and tracks based on the well-known Zhai method [34]. Consider in the simulation that the vehicle speed is 300 km/h and the wavelength and wave depth of rail irregularity are 10 m and 0.5 mm, respectively. Figure 3A shows the displacement of the car body calculated from the presented model and the Zhai model. The results of the wheel displacement are compared in Figure 3B. It can be observed that the numerical results of the two models are only slightly different. Therefore, the present vehicle-track interaction model is considered valid.

3. NUMERICAL ALGORITHMS

In this section, an interactive algorithm is proposed to couple the two sub-models. Therefore, there are three main interactive procedures in this solution algorithm. Two of them are used to deal with the nonlinear wheel-track dynamic interaction and the pantograph-overhead system dynamic interaction. The third is used to deal with the nonlinear behavior of each dropper working in tension or compression, as well as update the stiffness matrix of each cable element of messenger/contact line. The iterative procedure for the whole coupled system in each time step (from t to $t + \Delta t$) is presented as follows:

Table 3. Parameters of the high-speed track

Elastic modulus of rail (N/m²)	2.059×10^{11}
Area moment of rail cross-section (m⁴)	3.217×10^{-5}
Rail mass per unit length (kg/m)	60.64
Mass of half sleeper (kg)	170
Rail pad stiffness (N/m)	6.0×10^{7}
Rail pad damping (N s/m)	7.5×10^{4}
Sleeper spacing (m)	0.6
Effective support length of half sleeper (m)	1.175
Sleeper width (m)	0.277
Ballast density (kg/m³)	1.9×10^{3}
Elastic modulus of ballast (Pa)	1.2×10^{8}
Damping of ballast (N s/m)	6.0×10^{4}
Shear stiffness of ballast (N/m)	7.84×10^{7}
Shear damping of ballast (N s/m)	8.0×10^{4}
Ballast stress distribution angle (°)	35
Ballast thickness (m)	0.35
Subgrade K_{30} modulus (Pa/m)	1.9×10^{8}
Damping of subgrade (N s/m)	1.0×10^{5}

A: Car body displacement   B: Wheel displacement
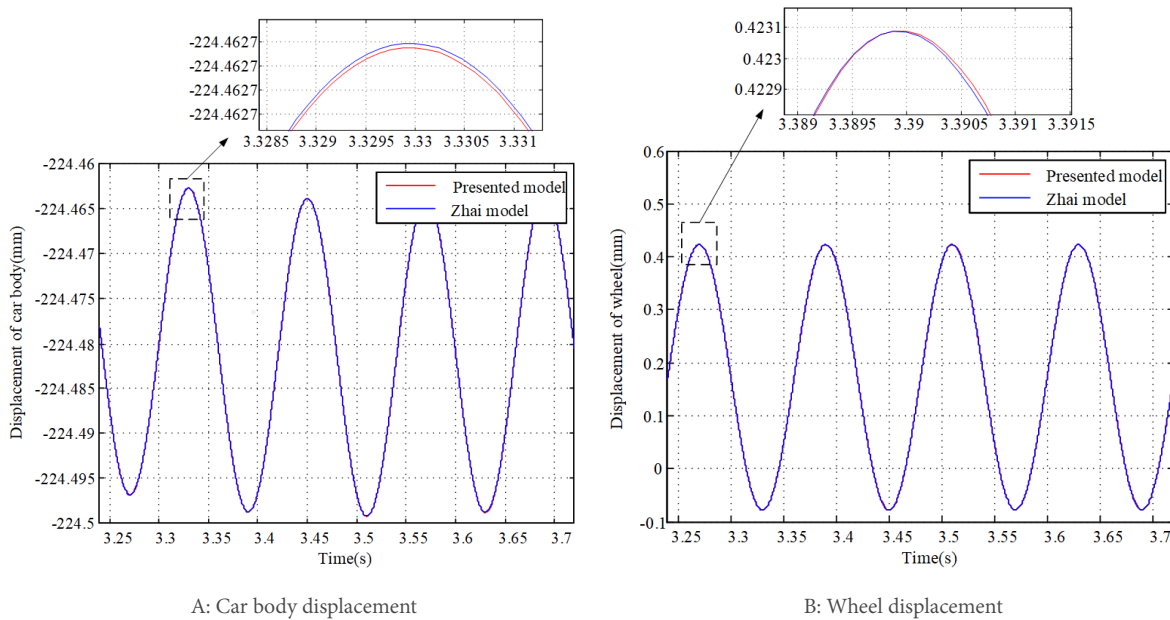
Figure 3. Verification of the vehicle-track model.

Step 1. Calculate the contact points of the pantograph-overhead system interaction and the vehicle-track interaction.

Step 2. Initialize the iteration count $k_1 = 0$ and the displacement vectors $\mathbf{X}_C^{k_1}(t + \Delta t) = \mathbf{X}_C(t)$, $\mathbf{X}_V^{k_1}(t + \Delta t) = \mathbf{X}_V(t)$, and $\mathbf{X}_T^{k_1}(t + \Delta t) = \mathbf{X}_T(t)$ for the overhead system, pantograph-vehicle, and track systems, respectively.

Step 3. Update the wheel-track forces $f_{wj}(t + \Delta t)$ by Equation (19) using $\mathbf{X}_V^{k_1}(t + \Delta t)$ and $\mathbf{X}_T^{k_1}(t + \Delta t)$.

Step 4. Exert the wheel-track forces $f_{wj}(t + \Delta t)$ on the track and solve Equation (17) to obtain $\mathbf{X}_T^{k_1+1}(t + \Delta t)$.

Step 5. Update the wheel-track forces $f_{wj}(t + \Delta t)$ by Equation (19) using $\mathbf{X}_V^{k_1}(t + \Delta t)$ and $\mathbf{X}_T^{k_1+1}(t + \Delta t)$.

Step 6. Exert the wheel-track force $f_{wj}(t + \Delta t)$ on the overhead system-pantograph-vehicle system to solve the overhead system displacement vector $\mathbf{X}_C^{k_1+1}(t + \Delta t)$ and the pantograph-vehicle displacement vector $\mathbf{X}_T^{k_1+1}(t + \Delta t)$(the detailed sub-steps are shown as *Steps 6-1-6-12*).

Step 6-1. Initialize the iteration count $k_2 = 0$, the overhead system displacement vector $\mathbf{X}_C^{k_2}(t + \Delta t) = \mathbf{X}_C^{k_1}(t + \Delta t)$, and the pantograph-vehicle displacement vector $\mathbf{X}_V^{k_2}(t + \Delta t) = \mathbf{X}_V^{k_1}(t + \Delta t)$.

Step 6-2. Calculate the contact force $f_c(t + \Delta t)$ using the overhead system displacement vector $\mathbf{X}_C^{k_2}(t + \Delta t)$

and pantograph-vehicle displacement vector $\mathbf{X}_V^{k_2}(t + \Delta t)$ based on the penalty method (Equation (18)).

Step 6-3. Update the nodal forces $f_1 \sim f_6$ and element stiffness matrix $\mathbf{K}_C^e$ of each cable element using overhead system displacement vector $\mathbf{X}_C^{k_2}(t + \Delta t)$ based on Equation (1). The Newton-Raphson iteration method is adopted here (the detailed sub-steps are listed as *Steps 6-3-1-6-3-6*).

Step 6-3-1. Calculate $l_x = x_j - x_i$, $l_y = y_j - y_i$, and $l_z = z_j - z_i$ of each cable element according to the global displacement $\mathbf{X}_C^{k_2}(t + \Delta t)$.

Step 6-3-2. Initialize the internal force vector $\mathbf{F}^e = \left\{ f_1 \quad f_2 \quad f_3 \right\}^T$ of each element.

Step 6-3-3. Calculate the relative positions l_x^*, l_y^*, and l_z^* using Equation (1).

Step 6-3-4. Calculate $\mathbf{dl} = \left\{ (l_x^* - l_x)(l_y^* - l_y)(l_z^* - l_z) \right\}$. If all elements of $\mathbf{dl}$ are smaller than the pre-set tolerance, formulate the element stiffness matrix $\mathbf{K}_C^e$ using Equation (5) and break out of the iteration; otherwise, continue to the next step.

Step 6-3-5. Calculate the correction vector of internal forces $\mathbf{dF}^e = \left\{ \mathrm{d}f_1 \quad \mathrm{d}f_2 \quad \mathrm{d}f_3 \right\}^T$ using Equation (6).

Step 6-3-6. Update the internal forces $\mathbf{F}^e = \mathbf{F}^e + \mathbf{dF}^e$ and go back to *Step 6-2-3*.

Step 6-4. Update the nodal forces $f_{g1} \sim f_{g6}$ and element stiffness matrix $\mathbf{K}_C^{eg}$ of each string element using overhead system displacement vector $\mathbf{X}_C^{k_2}(t + \Delta t)$ according to Equation (7). Here, the force state of each dropper is checked. If the dropper works in compression, $E_g A_g$ equals zero.

Step 6-5. Formulate the internal force vector $\mathbf{F}_r^{k_2}$ depending on the internal forces of each element ($f_1 \sim f_6$ and $f_{g1} \sim f_{g6}$).

Step 6-6. Use the internal force vector $\mathbf{F}_r^{k_2}$ and the contact force $f_c(t + \Delta t)$ to formulate the incremental excitation vector $\Delta \mathbf{F}_C^{k_2}(x, t)$ of overhead system.

Step 6-7. Formulate the global stiffness matrix $\mathbf{K}_C(t + \Delta t)$ of overhead system using each element stiffness matrix of cable and string according to the FEM.

Step 6-8. Exert the incremental excitation vector $\Delta \mathbf{F}_C^{k_2}(x, t + \Delta t)$ on overhead system and solve Equation (12) to obtain the incremental displacement vector $\Delta \mathbf{X}_C^{k_2}(x, t + \Delta t)$ of overhead system.

Step 6-9. Update the displacement vector $\mathbf{X}_C^{k_2+1}(x, t + \Delta t) = \mathbf{X}_C^{k_2}(x, t + \Delta t) + \Delta \mathbf{X}_C^{k_2}(x, t + \Delta t)$ of overhead system.

Step 6-10. Exert the pantograph-overhead system contact force $f_c(t + \Delta t)$ and the wheel-track contact force $f_{wj}(t + \Delta t)$ on pantograph-vehicle and solve Equation (13) to obtain the displacement vector $\mathbf{X}_V^{k_2+1}(x, t + \Delta t)$ of pantograph-vehicle.

Step 6-11. Check the convergence of the incremental displacement vectors $\Delta \mathbf{X}_C^{k_2}(x, t + \Delta t)$ and $\Delta \mathbf{X}_V^{k_2}(x, t + \Delta t) = \mathbf{X}_V^{k_2+1}(x, t + \Delta t) - \mathbf{X}_V^{k_2}(x, t + \Delta t)$. If the convergence criterion is satisfied, $\mathbf{X}_V^{k_1}(x, t + \Delta t) = \mathbf{X}_V^{k_2+1}(x, t + \Delta t)$ and $\mathbf{X}_C^{k_1}(x, t + \Delta t) = \mathbf{X}_C^{k_2+1}(x, t + \Delta t)$, and break out of the iteration. Otherwise, go to *Step 6-12*.

Step 6-12. Update the iteration count $k_2 = k_2 + 1$ and return to *Step 6-2*.

Step 7. Check the convergence of the incremental displacement vector $\Delta \mathbf{X}_T^{k_1}(x, t + \Delta t) = \mathbf{X}_T^{k_1+1}(x, t + \Delta t) - \mathbf{X}_T^{k_1}(x, t + \Delta t)$ of track. If the convergence criterion is satisfied, go to *Step 8*. Otherwise, Update the iteration count $k_1 = k_1 + 1$ and return to *Step 3*.

Step 8. Update the acceleration vectors and velocity vectors of overhead system, track, and vehicle-track systems according to Newmark method. Enter the next time step $t = t + \Delta t$.

It should be noted that the mass of vehicle is several orders of magnitude higher than the pantograph, and the effect of pantograph vibration on the car body can be neglected. In this work, we investigate the pantograph-overhead system interaction with the perturbations of vehicle-track and achieve an accurate simulation result. This interaction between the pantograph and the vehicle is also considered in the simulation. As indicated in [36], the choice of numerical integrator and the time-space discretization has a significant effect on the numerical results. In this paper, the frequency of interest is limited to 0-20 Hz. A high sampling frequency of 2000 Hz is adopted in the numerical simulation to ensure numerical stability. The element size in the contact wire is set as 0.25 m to ensure that numerical error cannot affect the results in the frequency range of interest.

A
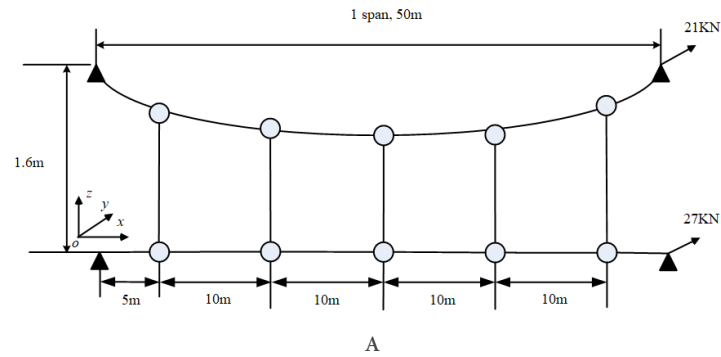
- Contact wire: line density (1.082 kg/m), tensile rigidity (10^6 N/m).
- Messenger wire: line density (1.068 kg/m), tensile rigidity (10^6 N/m).
- Dropper: line density (0.14), tensile rigidity (10^5 N/m).
- Stagger (± 0.2 m).
- Installation height (5.3 m).
- Encumbrance (1.6 m).
- Max contact wire reserved pre-sag (0.5‰ × span).

B
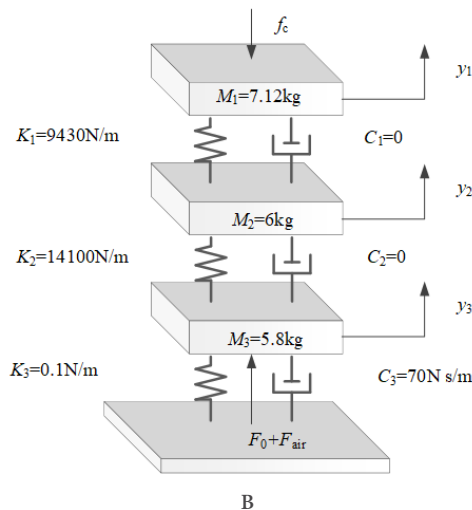
Figure 4. Parameters of the pantograph-overhead system: (A) geometry information of a simple overhead system model; and (B) three-DOF model of a pantograph.

4. NUMERICAL ANALYSIS

To reveal the influence of the vehicle-track vibration on the pantograph-overhead system interaction, a whole coupled dynamics model for the railway system is established according to the description in Section 2. The parameters of a high-speed overhead system constructed in China are adopted, as shown in Figure 4A. The lumped parameters of the DSA-380 pantograph are given in Figure 4B. The parameters in Table 1 and Table 2 are adopted for the high-speed vehicle-track model. The flow chart of the subsequent analysis is presented in Figure 5.

4.1. Influence of specific rail irregularity
This section mainly focuses on the analysis of the influence of the rail irregularity with specific wavelength and wave depth on the pantograph-overhead system interaction. The rail irregularity can be described as [37]

$$w_0(t) = \frac{1}{2}a\left(1 - \cos\frac{2\pi v}{l}t\right) \qquad 0 \le t \le \frac{L}{v} \qquad (20)$$
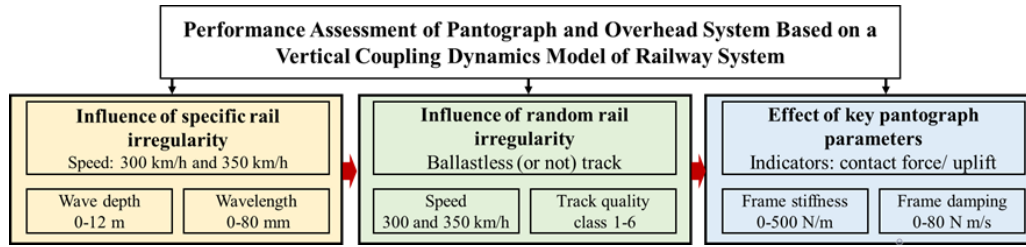
Figure 5. Flow chart of analysis in this paper.

A. $v = 300$ km/h $l = 15$ mm

B. $v = 300$ km/h $l = 60$ mm

C. $v = 350$ km/h $l = 15$ mm

D. $v = 350$ km/h $l = 60$ mm
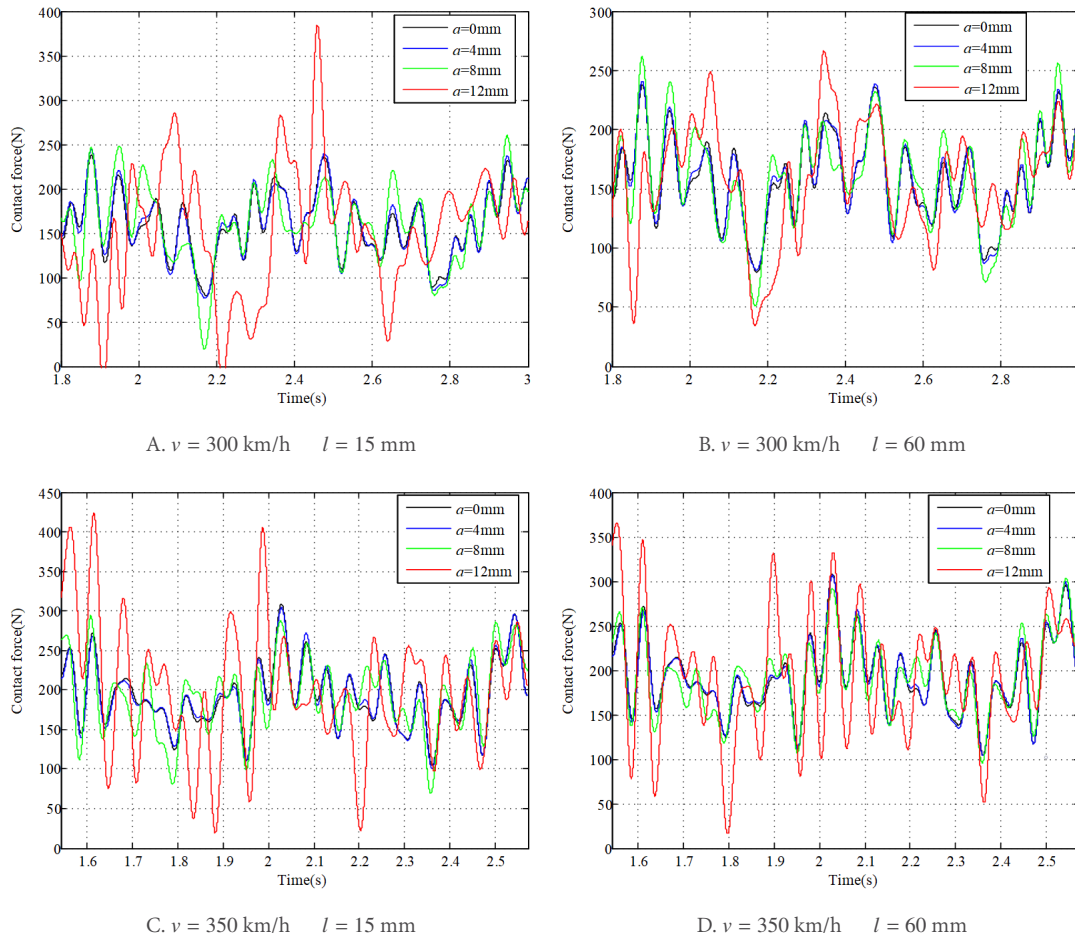
Figure 6. Results of contact force at different wave depths of rail irregularity.

where v is the vehicle speed, a is the wave depth of the track irregularity, l is the wavelength of the track irregularity, and L is the length of the track.

The response of the high-speed overhead system-pantograph-vehicle-track is solved by employing the iterative algorithms proposed in Section 3.

The resulting contact force of the pantograph-overhead system with different wave depths of rail irregularity is shown in Figure 6A-D, in which the vehicle speeds are 300 and 350 km/h and the wavelengths of rail irregularity are 15 and 60 mm, respectively. All the results of contact force are filtered in the frequency range of interest from 0 to 20 Hz. It can be observed that the increase of the wave depth of rail irregularity leads to a significant
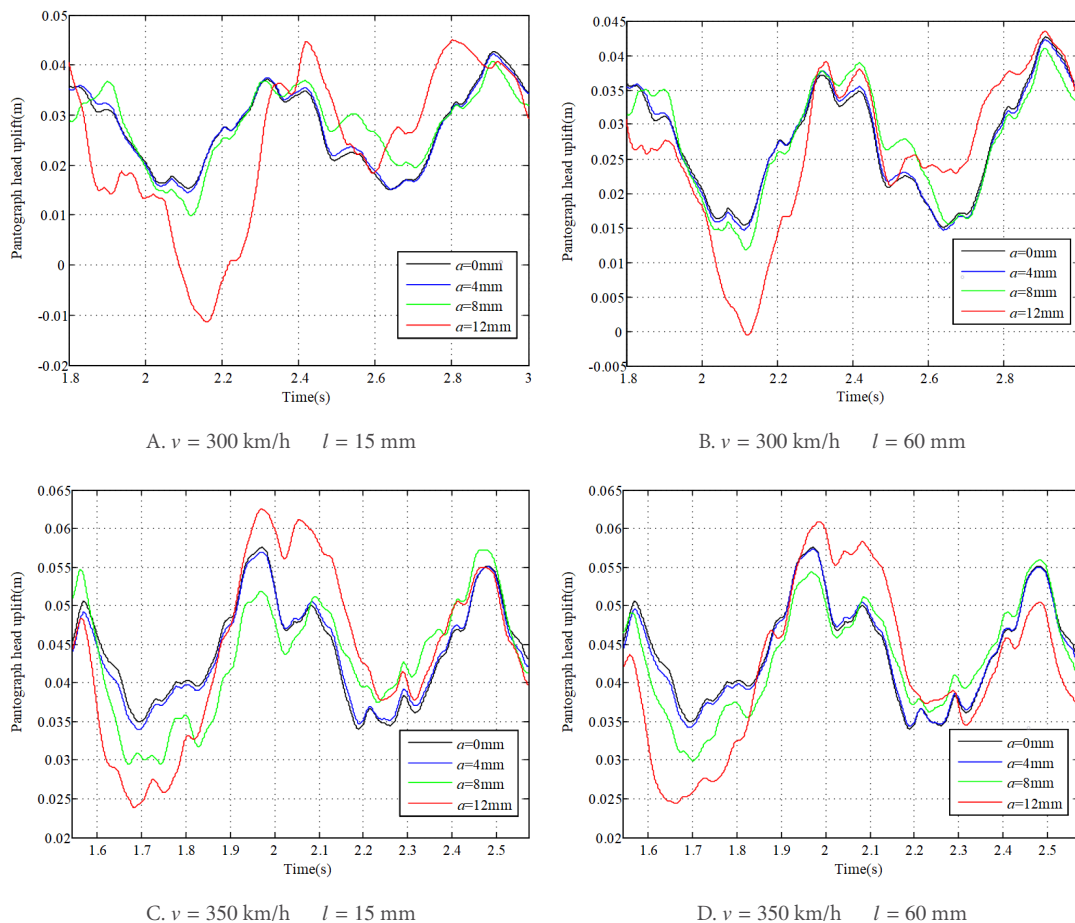
Figure 7. Results of pantograph head uplift at different wave depths of rail irregularity.

increase of the fluctuation in contact force between the pantograph and the overhead system. When the wave depth increases from 0 to 8 mm, the waveforms of the contact force are similar at the two different vehicle speeds, while the fluctuation in contact force increases. However, when the irregularity wave depth increases up to 12 mm, the waveform of contact force undergoes a big change and a bigger fluctuation in contact force can be observed. In particular, at the wave depth of 12 mm, contact loss can be found and the maximum contact force reaches 380 N in Figure 6A. The overall maximum value of contact force appears in Figure 6C, which reaches more than 420 N.

The corresponding results of the pantograph head uplift and the contact wire deflection at contact point are shown in Figure 7A-D and Figure 8A-D, respectively. The structural characteristics of the overhead system can be observed obviously from the vibration of the pantograph head, as well as the displacement of the contact wire. Similar to the contact force, the vibrations of the pantograph head and the contact wire also experience continuous increases with the increase of the wave depth of rail irregularity. The minimum values of the pantograph head uplift and the contact wire deflection appear in Figure 7A and Figure 8A, respectively, when the irregularity wave depth increases to 12 mm at a vehicle speed of 300 km/h. The maximum values appear in Figure 7C and Figure 8C at a vehicle speed of 350 km/h and an irregularity wavelength of 15 mm.

To evaluate the influence of the rail irregularity wave depth on the current collection of the pantograph-overhead system, the standard deviation of contact force is shown in Figure 9 at different wave depths of rail irregularity. It is found that the standard deviation increases continuously with the increase of the wave

A. v = 300 km/h l = 15 mm

B. v = 300 km/h l = 60 mm

C. v = 350 km/h l = 15 mm

D. v = 350 km/h l = 60 mm
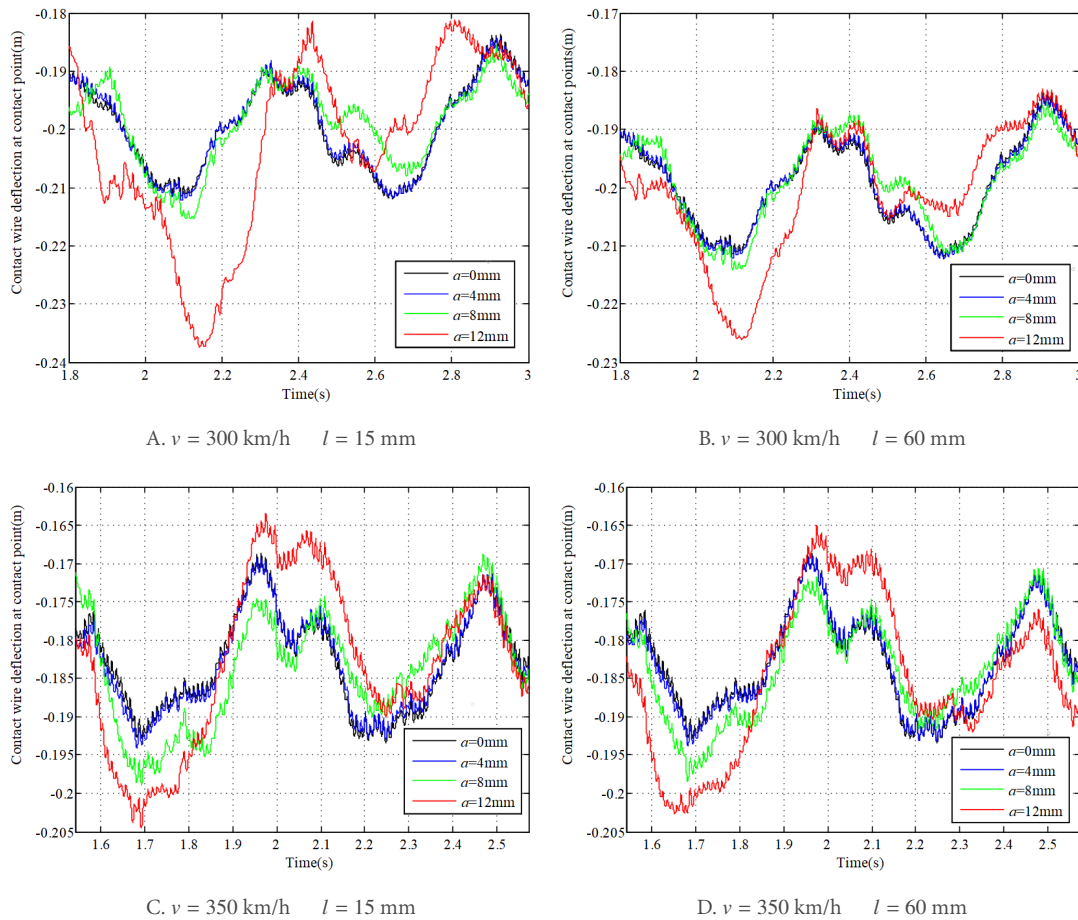
Figure 8. Results of contact wire deflection at contact point at different wave depths of rail irregularity.

depth of rail irregularity. Especially when it reaches 6 mm, the standard deviation shows a sharp increase. It can be concluded that the increase of the wave depth of the rail irregularity can lead to a significant increase of the fluctuation in contact force, which may result in the deterioration of current collection of the pantograph-overhead system.

Apart from the analysis of the dynamic performance at wave depths of rail irregularity, the following investigation mainly focuses on revealing the influence of the wavelength of rail irregularity on the pantograph-overhead system interaction. Suppose that the wave depth of rail irregularity is 10 mm, and the vehicle speeds are 300 and 350 km/h, respectively. The results of the contact force with different wavelengths of rail irregularity are shown in Figure 10A,B. It is found that, although the wave depth of rail irregularity remains unchanged, the contact force changes with the wavelength of rail irregularity at each vehicle speed.

The corresponding results of the pantograph head uplift and the contact wire deflection are shown in Figure 11A,B and Figure 12A,B, respectively. The difference in the dynamic response with different wavelengths of rail irregularity can be observed obviously. The vibrations of the pantograph head and contact wire are different at different wavelengths of rail irregularity. The results of the standard deviation of contact force at different wavelengths of rail irregularity are plotted in Figure 13. It can be observed that the standard deviation changes much with different wavelengths of rail irregularity. Generally, the trends of the standard deviation with respect to the irregularity wavelength at different vehicle speeds are similar. The maximum value reaches 55.6 and 47.9 N with the same irregularity wavelength of 80 mm at vehicle speeds of 350 and 300 km/h, re-
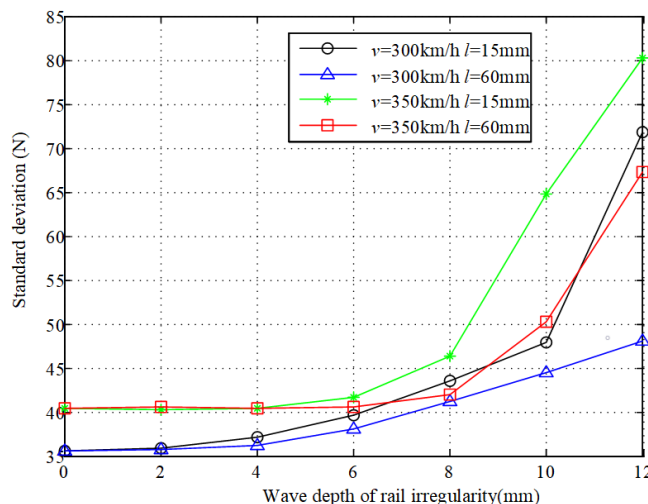
Figure 9. Standard deviation and statistical minimum value of contact force at different wave depths of rail irregularity.

A. *v* = 300 km/h   *a* = 10 mm   B. *v* = 350 km/h   *a* = 10 mm
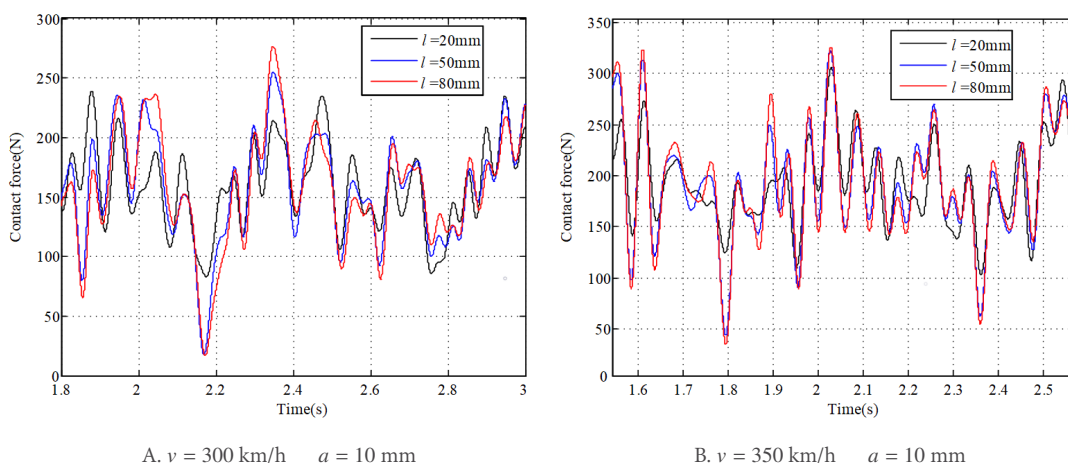
Figure 10. Results of contact force at different wavelengths of rail irregularity.

spectively. The overall minimum value of the standard deviation of contact force can be found in the case with the irregularity wavelength of 20 mm, which may ensure a relatively good current collection quality for the pantograph-overhead system. Thus, it can be concluded that both the wave depth and wavelength of rail irregularity seriously affect the interaction performance. Therefore, it is necessary to include them in the simulation and design of overhead system-pantograph for high-speed trains. It is also important to determine any rail irregularity wavelength that is detrimental to the current collection, which should be investigated in the future.

It is well known that rail irregularity can lead to vibration of the car body. Figure 14A shows the displacement of the car body with the rail irregularity wavelength of 15 mm and wave depth of 10 mm at a vehicle speed of 300 km/h. A spectral estimation method is utilized to analyze the frequency characteristics, as shown in Figure 14B. The spatial frequency with the highest power appears at 0.067 m^{-1}, which corresponds to a wavelength of 15 mm. The influence of the rail irregularity on the pantograph-overhead system can be considered as an external perturbation exerted on the bottom of the pantograph. The corresponding displacement of the pantograph head is shown in Figure 15A in parallel with the displacement calculated without rail irregularity. Their power spectrums of the pantograph head uplift are shown in Figure 15B. It can be observed that the significant peak

A. *v* = 300 km/h　　*a* = 10 mm　　　　　　　　B. *v* = 350 km/h　　*a* = 10 mm
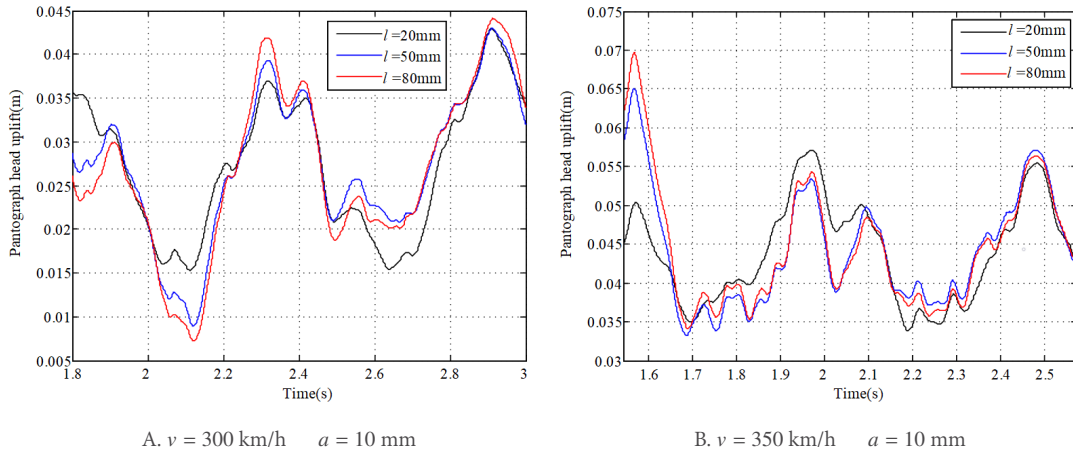
Figure 11. Results of pantograph head uplift at different wavelengths of rail irregularity.

A. *v* = 300 km/h　　*a* = 10 mm　　　　　　　　B. *v* = 350 km/h　　*a* = 10 mm
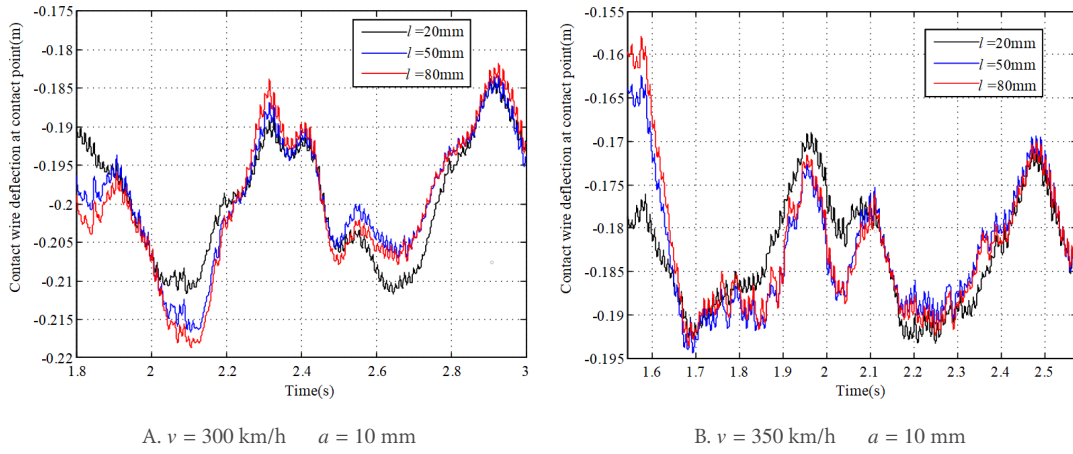
Figure 12. Results of contact wire deflection at contact point at different wavelengths of rail irregularity.
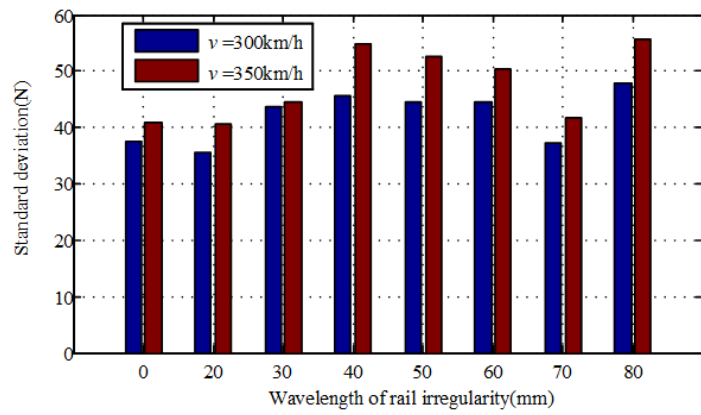
Figure 13. Results of standard deviation of contact force at different wavelengths of rail irregularity.

of the power spectrums appears at 0.02 m^{-1}, which corresponds to the span of overhead system. The frequency of the interval of droppers can also be observed (about 0.1 m^{-1}). Although the rail irregularity changes the spectral power distribution of the pantograph head displacement to some extent, the frequency characteristics of the rail irregularity cannot be significantly observed from the power spectrum of the pantograph head uplift.

A. Car body displacement   B. Power spectrum
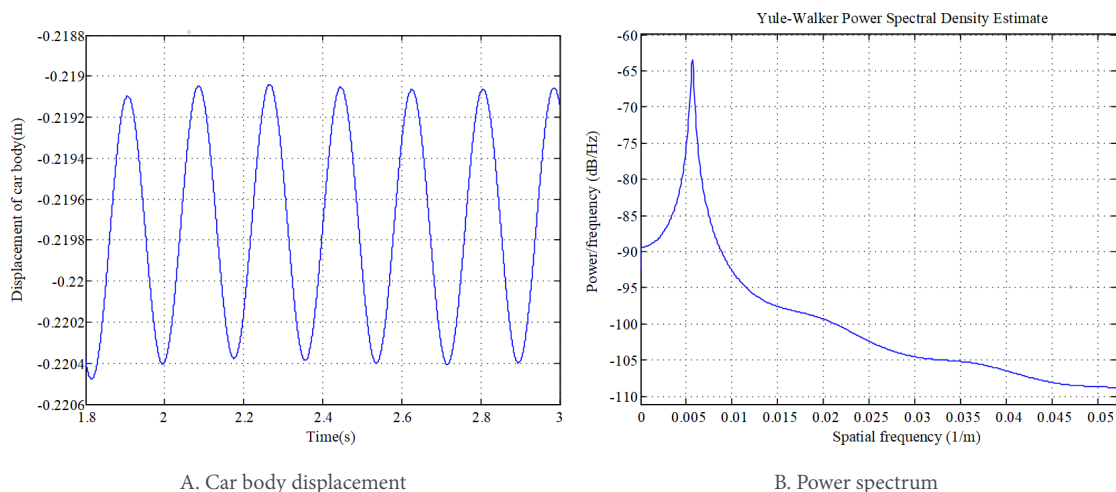
Figure 14. Car body displacement and its power spectrum.

A. Pantograph head uplift   B. Power spectrum
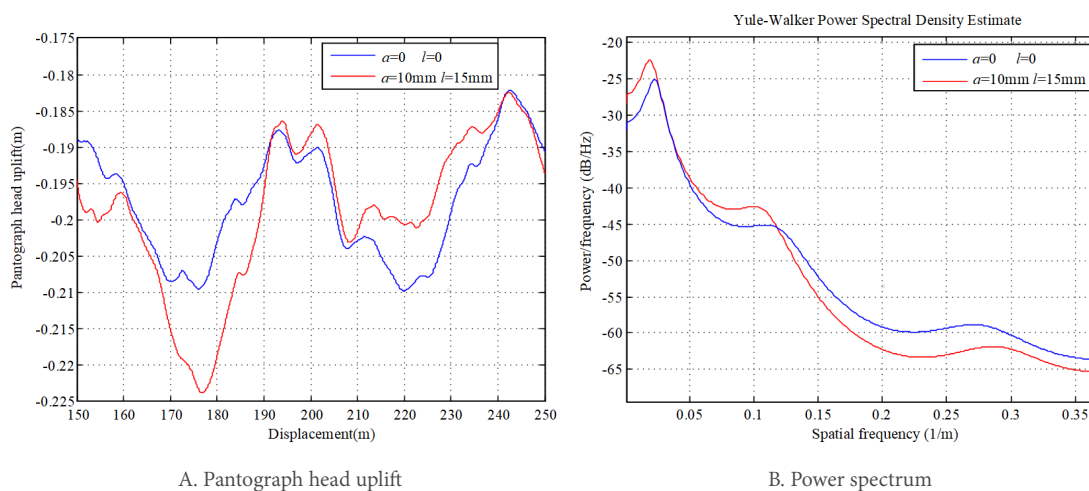
Figure 15. Pantograph head uplift and its spectral estimation.

4.2. Influence of random rail irregularity

The irregularity of a real track can be considered a random variable. In this section, the random rail irregularity is included in the track model, and its influence on the pantograph-overhead system interaction is studied. The track irregularity can be split up from the lowest (1) to the highest (6) quality classes [24] to study the dynamics of pantograph and overhead system interaction. The PSD function of the rail irregularity with different levels is presented in Table 4. The results of the contact force, pantograph head uplift, and contact wire deflection with different types of track irregularity are shown in Figures 16-18, respectively. Figure 16 shows that the contact force with the lowest-quality track fluctuates more compared with the others at each vehicle speed. A similar conclusion can be obtained for pantograph head uplift and contact wire deflection [Figure 17 and Figure 18]. The vibrations of the contact wire and the pantograph head with the lowest-quality track are significantly larger than others, which may exert a negative influence on the current collection. It is obvious that, due to the low quality of track, not only the maximum values of the vertical displacements of pantograph head and contact wire increase, but also the minimum values decrease.

The results of standard deviation of contact force with different qualities of track irregularities at vehicle speeds of 300 and 350 km/h are shown in Figure 19. It can be observed that the fluctuation in contact force shows

Table 4. Coefficients of rail irregularities with different rail levels

Coefficient		Rail quality level					
		1	2	3	4	5	6
PSD of rail irregularity $S_v(\phi) = \frac{A_v \phi_{v2}^2(\phi^2+\phi_{v1}^2)}{\phi^4(\phi^2+\phi_{v2}^2)}$	$A_V/(10^{-7}$ m$)$	16.72	9.53	5.29	2.96	1.67	0.95
	$\phi_{v1}/(10^{-2}$ m$)$	2.33	2.33	2.33	2.33	2.33	2.33
	$\phi_{v2}/(10^{-1}$ m$)$	1.31	1.31	1.31	1.31	1.31	1.31

A. $v = 300$ km/h　　　　　　　　　　　B. $v = 350$ km/h
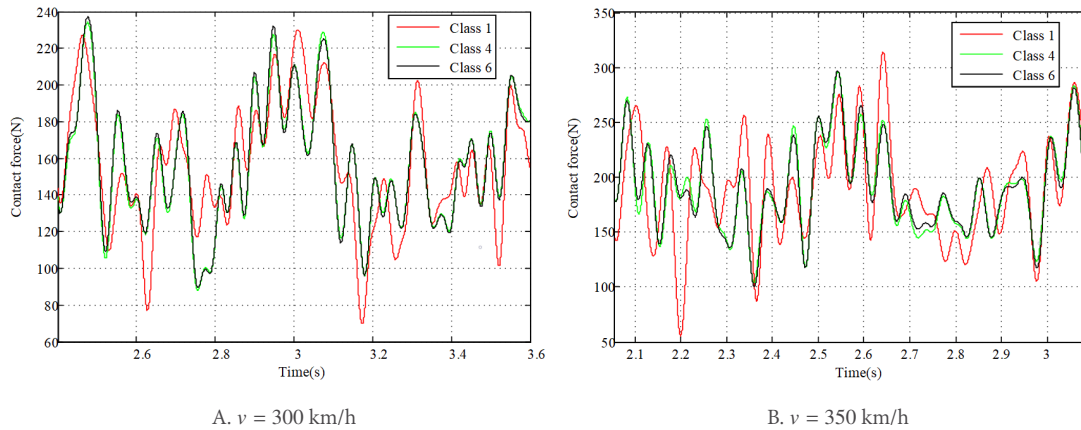
Figure 16. Results of contact force with different types of track irregularities.

A. $v = 300$ km/h　　　　　　　　　　　B. $v = 350$ km/h
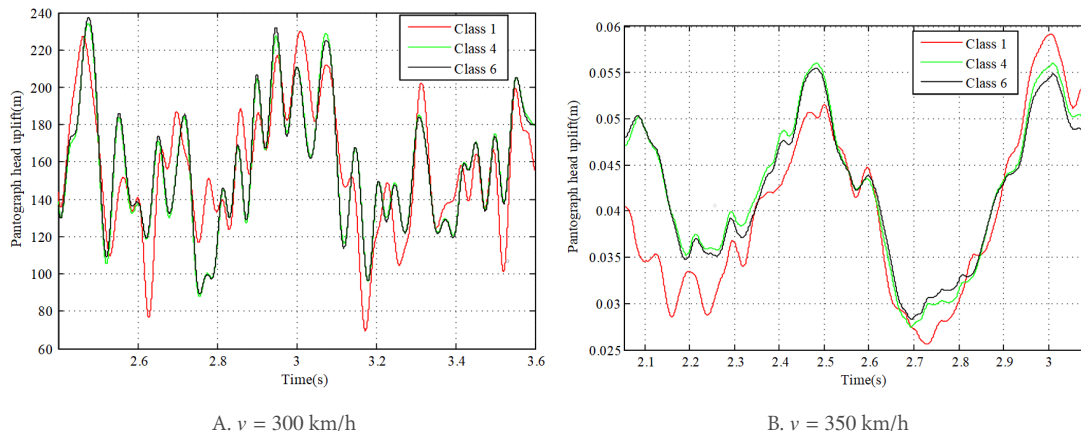
Figure 17. Results of pantograph head uplift with different types of track irregularities.

a continuous decrease with the improvement of the rail quality. For the quality class of 2-6, the standard deviation of contact force does not experience a significant change, which means that the influence of the random track irregularity is not as significant as the track irregularity with specific wave depth and wavelength. This conclusion is consistent with that found in [24].

Ballastless track is widely used in modern high-speed railway systems, in which the elasticity of track is mainly provided by the rail pad, as shown in Figure 20. This kind of track is designed to ensure a more stable operation of high-speed vehicles compared with the traditional track. Hence, the influence of the vehicle-ballastless track vibration on the pantograph-overhead system dynamic response is investigated compared with the traditional track. Consider that the quality level of track irregularities is 1 and the vehicle speeds are 300 and 350 km/h, respectively.

A. *v* = 300 km/h   B. *v* = 350 km/h
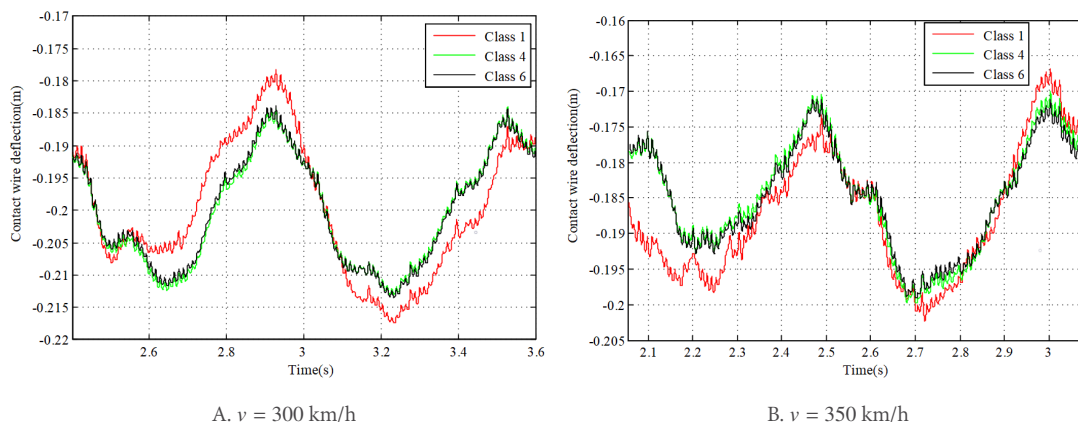
Figure 18. Results of contact wire deflection at contact point with different types of track irregularities.
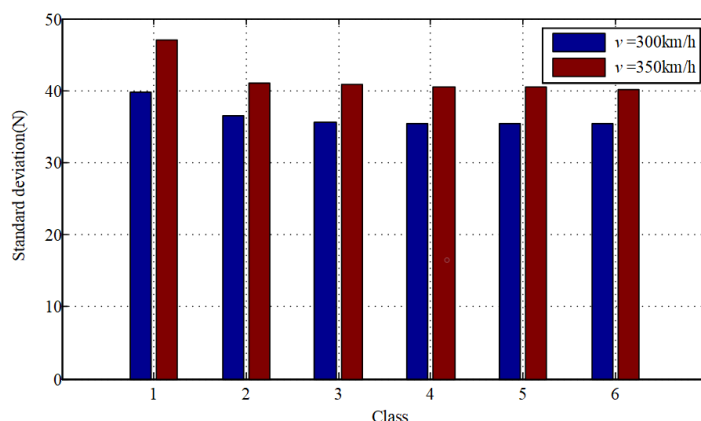

Figure 19. The results of standard deviation of contact force with different qualities of track irregularities.
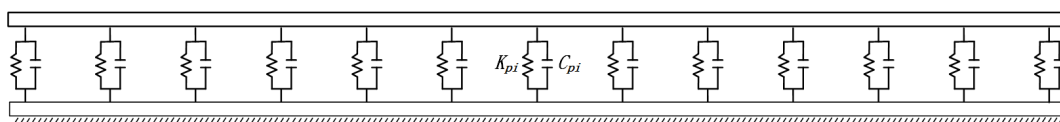

Figure 20. Ballastless track.

The results of contact force calculated with the traditional track and the ballastless track are compared in Figure 21. It can be observed that, at each vehicle speed, the results of contact force calculated with different kinds of tracks do not exhibit a large difference. However, by comparing the results of the pantograph head uplift [Figure 22], as well as the contact wire deflection at contact point [Figure 23], one can observe that the ballastless track can reduce the vibration of the pantograph head and the contact wire slightly. The standard deviations of contact force with the traditional track and the ballastless track are compared in Figure 24. They experience slight decreases of 0.26 and 0.43 N at 300 and 350 km/h, respectively, when the ballastless track is used. Thus, the ballastless track can make a small contribution to improving the current collection quality for high-speed pantograph-overhead system, in comparison with the traditional track.

The lower frame stiffness K_3 and damping C_3 serve as the connector between the vehicle and pantograph, which determines the vibration transmission from the vehicle-track to the pantograph-overhead system. In the previous studies, the influence of parameters of pantograph on the contact force is studied without consid-

A. *v* = 300 km/h

B. *v* = 350 km/h
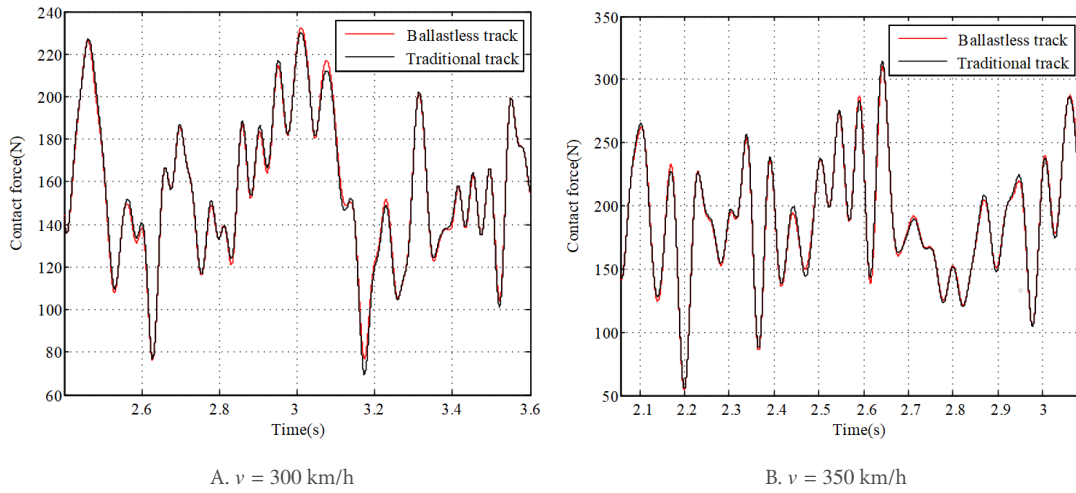
Figure 21. Comparison of contact force between traditional tack and ballastless track.

A. *v* = 300 km/h

B. *v* = 350 km/h
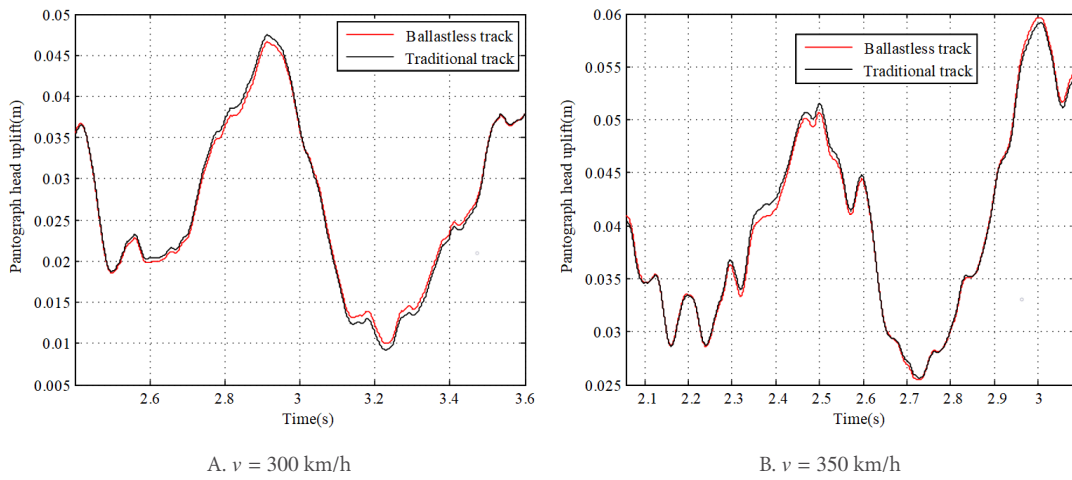
Figure 22. Comparison of pantograph head uplift between traditional tack and ballastless track.


A. *v* = 300 km/h

B. *v* = 350 km/h
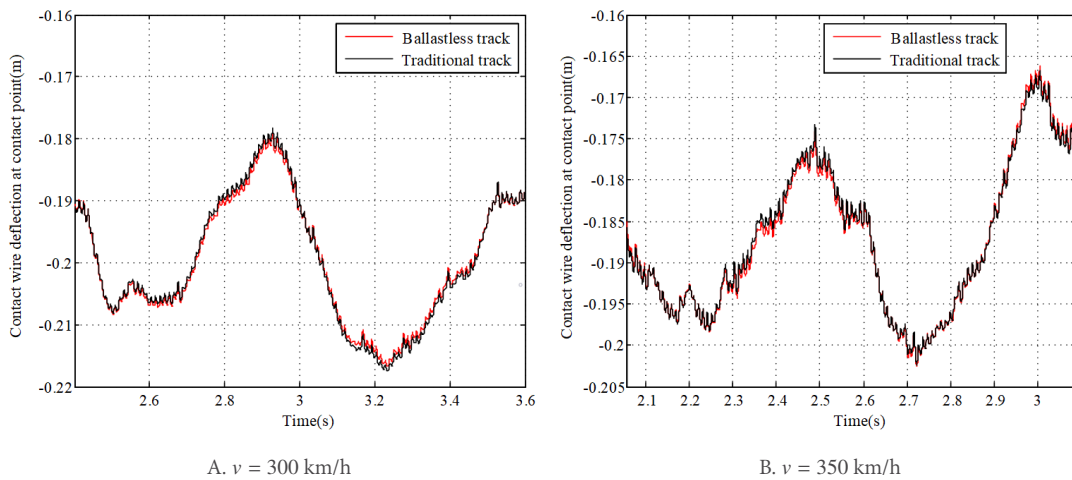
**Figure 23.** Comparison of contact wire deflection at contact point between traditional tack and ballastless track.
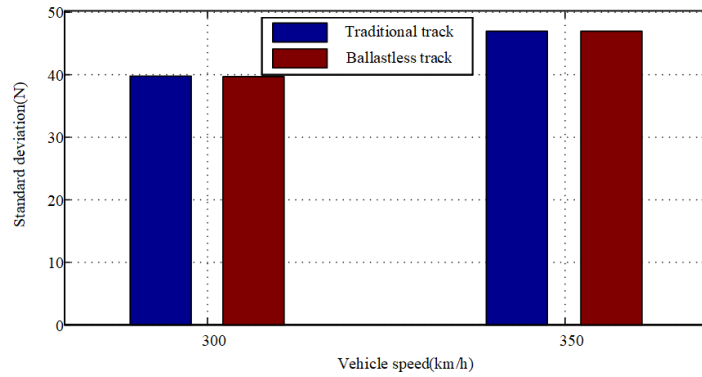
**Figure 24.** Results of standard deviation of contact force with traditional tack and ballastless track.

A. Contact force

B. Pantograph head uplift

C. Contact wire deflection

D. Standard deviation
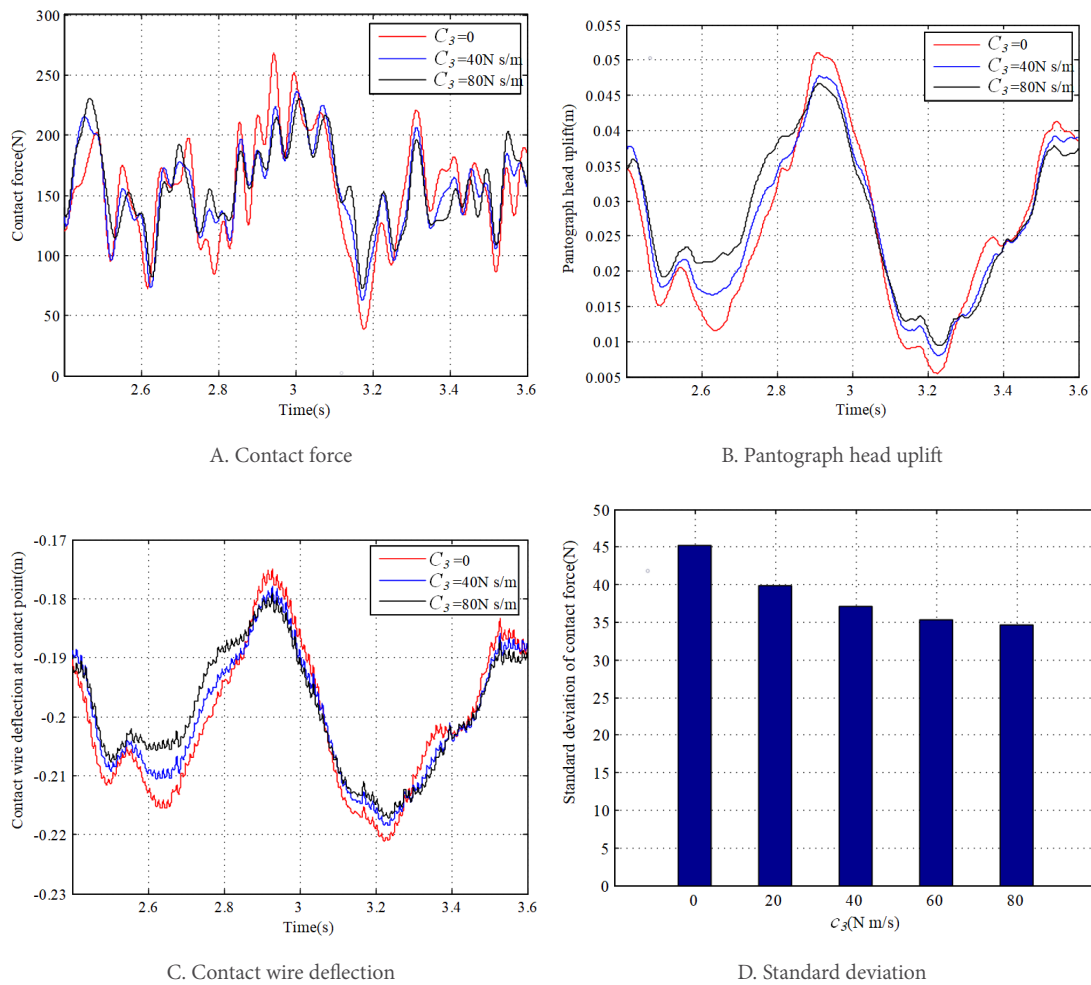
Figure 25. Results of the pantograph and overhead system dynamic response with different C_3.

ering the locomotive vibration [38,39]. In this paper, the influence of parameters K_3 and C_3 on the pantograph-overhead system interaction is studied. Consider that the vehicle speed is 300 km/h and the quality class of track irregularity is 1. The results of contact force with different C_3 are compared in Figure 25A. It is found that the lower frame damping C_3 has a noticeable effect on the contact force, and it reduces contact force fluctuation [Figure 25D]. This damping is seen to have the same vibration effect on the pantograph head and contact wire [Figure 25B,C] and thus is able to improve the current collection quality.

A. Contact force

B. Pantograph head uplift

C. Contact wire deflection

D. Standard deviation
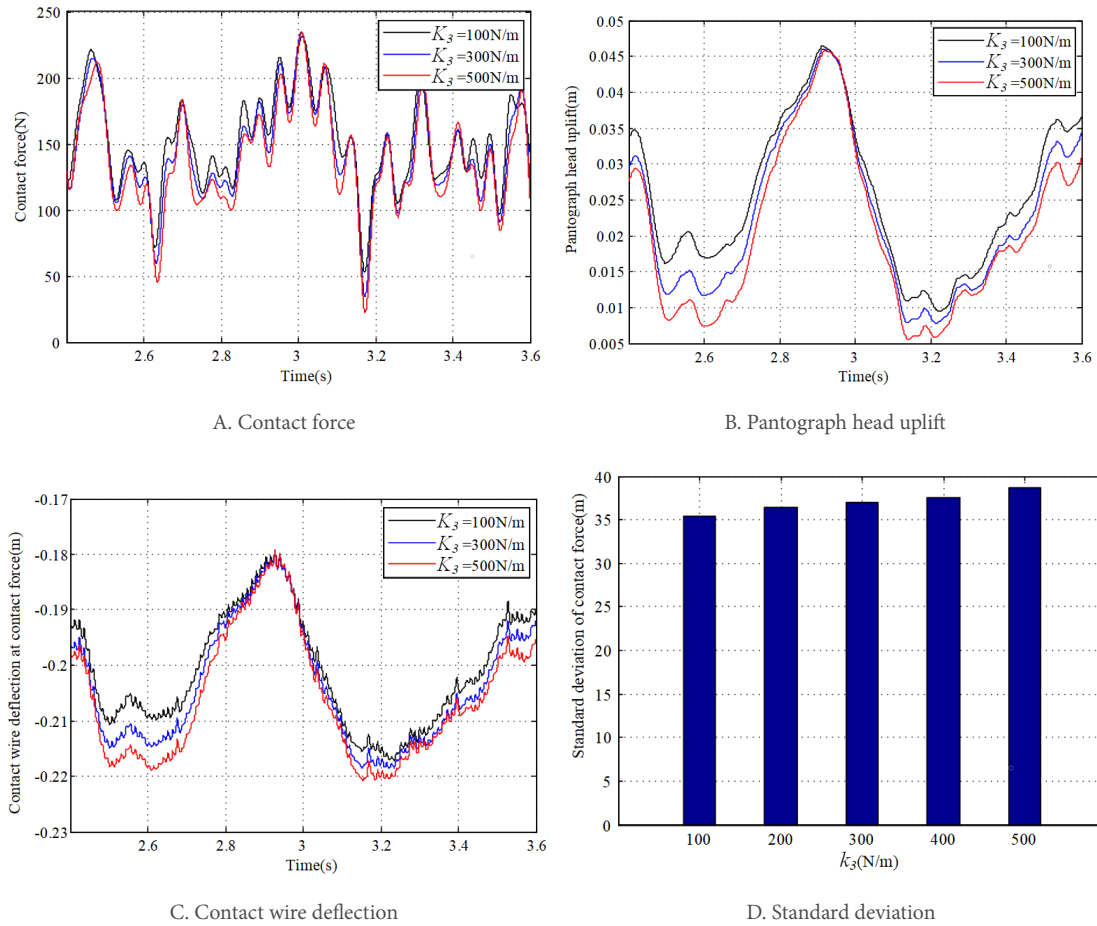
Figure 26. Results of the pantograph-overhead system dynamic response with different K_3.

The results of dynamic response with different K_3 are shown in Figure 26A-D. It is clear that the increase of the lower frame stiffness K_3 leads to a noticeable increase of the fluctuation in contact force [Figure 26A], pantograph head uplift [Figure 26B], and contact wire deflection [Figure 26C]. The standard deviation of the contact force shows a continuous increase with the increase of K_3 [Figure 26D]. It can be explained that the increase of K_3 enhances the transmission of vibration from the track vehicle to the pantograph. Thus, a large K_3 is not good for maintaining a stable current collection for the pantograph-overhead system.

5. CONCLUSIONS

This paper mainly focuses on the analysis of the influence of vehicle-tack vibration on the dynamic behavior of the pantograph-overhead system for the modern high-speed railway. A whole coupling model of railway system is established. A numerical algorithm for solving the coupled model is proposed, which is realized by the combination of the nonlinear finite element procedure for the pantograph-overhead system and the solution procedure for the vehicle-track dynamics. The influence of the vehicle-track vibration on the pantograph-overhead system interaction is studied through several numerical examples. The conclusions can be summarized as follows:

(1)The increase of the track irregularity wave depth leads to the increase of the fluctuation in contact force and the vibration of the pantograph-overhead system, which may aggravate the current collection.
(2) The wavelength of track irregularity exerts a noticeable effect on the dynamic behavior of pantograph-

overhead system. It is necessary to find the wavelength of track irregularity which is detrimental to the current collection in future works.

(3) The frequency characteristics of the rail irregularity can be detected from the car body response significantly, which cannot be observed from the power spectrum of the dynamic response of the pantograph head uplift.

(4) A higher-quality track is more beneficial to the pantograph-overhead system current collection compared to a lower-quality track.

(5) The use of the ballastless track can slightly improve the current collection of the pantograph-overhead system.

(6) The increase of C_3 can suppress the vibration of the pantograph and overhead system. A smaller K_3 is better for the current collection of the pantograph-overhead system. This investigation may provide a beneficial reference for the optimization of the pantograph-overhead system considering the vehicle-track vibration.

It should be noted that the lumped mass model of the pantograph used in this paper is a physical representation of the first several critical modes of a realistic one. The adopted model can only consider the effect of very low-frequency effect of vehicle-track vibration on the pantograph-overhead system interaction. A multibody dynamics model that fully describes the geometrical configuration of a pantograph is desired to capture a more realistic effect of vehicle-track perturbations on the pantograph-catenary system.

DECLARATIONS

Authors' contributions
Made substantial contributions to conception and design of the study and performed data analysis and interpretation: Song Y
Performed data acquisition, as well as providing administrative and simulation support: Duan F

Availability of data and materials
Not applicable.

Conflicts of interest
All authors declared that there are no conflicts of interest.

Ethical approval and consent to participate
Not applicable.

Consent for publication
Not applicable.

REFERENCES

1. Li Z, Chen J, Deng J. A feedforward air-conditioning energy management method for high-speed railway sleeper compartment. *Complex Eng Syst* 2022;2. DOI
2. Lu Z, Wang X, Yue K, Wei J, Yang Z. Coupling model and vibration simulations of railway vehicles and running gear bearings with multitype defects. *Mech Mach Theory* 2021;157:104215. DOI

3. Wang C, Zhang Q, Li H, Zhang L, Zhang B. Warpage deformation behavior of metal laminates. *Chinese J Eng* 2021;43:409-21. (In Chese) DOI

4. Tang W, Ma H, Yuan Y, Liu Z, Yu Z. Investigation on the influence of Cu-Al2O3 dispersion copper high-speed railway contact wire on current-collecting quality of pantograph-catenary. *J Railw Sci Eng* 2021;18:1098-104. DOI

5. Luo L, Ye W, Wang J. Defect detection of the puller bolt in high-speed railway catenary based on deep learning. *J Railw Sci Eng* 2021;18:605-14. DOI

6. Gao SB, Liu ZG, Yu L. Detection and monitoring system of the pantograph-catenary in high-speed railway (6C). In 2017 7th international conference on power electronics systems and applications - smart mobility, power transfer & security (PESA), Hong Kong, China, 12-14 December 2017; pp. 1-7 DOI

7. Xu Z, Gao G, Yang Z, Wei W, Wu G. An online monitoring device for pantograph catenary arc temperature detect based on atomic emission spectroscopy. In 2018 IEEE international conference on high voltage engineering and application (ICHVE) 2018; pp. 1-4. DOI

8. Zhang Y, Yue Y, Zhao S, Sihua W. Research on galloping response of catenary positive feeder in gale area considering surface roughness of stranded wire. *J Railw Sci Eng* 2021;18:1885-94. DOI

9. Song Y, Liu Z, Wang H, Lu X, Zhang J. Nonlinear analysis of wind-induced vibration of high-speed railway catenary and its influence on pantograph - catenary interaction. *Veh Syst Dyn* 2016;54:723-47. DOI

10. Zhang W, Zou D, Tan M, Zhou N, Li R, Mei G. Review of pantograph and catenary interaction. *Front Mech Eng* 2018;13:311-22. DOI

11. Liu Z, Song Y, Han Y, Wang H, Zhang J, Han Z. Advances of research on high-speed railway catenary. *J Mod Transp* 2018;26:1-23. DOI

12. Song Y, Liu Z, Wang H, Lu X, Zhang J. Nonlinear modelling of high-speed catenary based on analytical expressions of cable and truss elements. *Veh Syst Dyn* 2015;53:1455-79. DOI

13. Yao Y, Zhou N, Mei G, Zhang W. Dynamic Analysis of Pantograph-Catenary System considering Ice Coating. *Shock Vib* 2020;1-15. DOI

14. Tur M, García E, Baeza L, Fuenmayor FJ. A 3D absolute nodal coordinate finite element model to compute the initial configuration of a railway catenary. *Eng Struct* 2014;71:234-43. DOI

15. Bautista A, Montesinos J, Pintado P. Dynamic interaction between pantograph and rigid overhead lines using a coupled FEM - Multibody procedure. *Mech Mach Theory* 2016;97:100-11. DOI

16. Lu X, Liu Z, Song Y, Wang H, Zhang J, Wang Y. Estimator-based multiobjective robust control strategy for an active pantograph in high-speed railways. *J Rail Rapid Transit* 2018;232:1064-77. DOI

17. Gregori S, Tur M, Nadal E, Fuenmayor FJ. An approach to geometric optimisation of railway catenaries. *Veh Syst Dyn* 2018;56:1162-86. DOI

18. Wang W, Liang Y, Zhang W, Iwnicki S. Effect of the nonlinear displacement-dependent characteristics of a hydraulic damper on high-speed rail pantograph dynamics. *Nonlinear Dyn* 2019;95:3439-64. DOI

19. Liu Z, Liu W, Han Z. A high-precision detection approach for catenary geometry parameters of electrical railway. *IEEE Trans Instrum Meas* 2017;66:1798-808. DOI

20. Han Y, Liu Z, Geng X, Zhong J. Fracture Detection of Ear Pieces in Catenary Support Devices of High-speed Railway Based on HOG Features and Two-Dimensional Gabor Transform. *J China Railw Soc* 2017;39:52-7. (In Chinese) DOI

21. Liu W, Liu Z, Li Y, Wang H, Yang C, Wang D, Zhai D. An automatic loose defect detection method for catenary bracing wire components using deep convolutional neural networks and image processing. *IEEE Trans Instrum Meas* 2021;70:1-14. DOI

22. Cheng H, Wang J, Liu J, Cao Y, Li H, Xu X. Comprehensive evaluation method of catenary status based on improved multivariate statistical control chart. *J Railw Sci Eng* 2021;18:3048-56. DOI

23. Wang H, Nunez A, Liu Z, Zhang D, Dollevoet R. A Bayesian Network Approach for Condition Monitoring of High-Speed Railway Catenaries. *IEEE Trans Intell Transp Syst* 2020;21:4037-51. DOI

24. Song Y, Wang Z, Liu Z, Wang R. A spatial coupling model to study dynamic performance of pantograph-catenary with vehicle-track excitation. *Mech Syst Signal Process* 2021;151:107336. DOI

25. Ma H, Zhang D, Yi Y. Influence of the soft reduction process on the sensitivity of the inner crack in heavy rail steel bloom. *Chinese J Eng* 2021;43:1679-88. DOI

26. Qin R, Zhu B, Qiao K, Wang D, Sun N, Yuan X. Simulation study of the protective performance of composite structure carbon fiber bulletproof board. *Chinese J Eng* 2021;43:1346-54. DOI

27. Bruni S, Ambrosio J, Carnicero A, et al. The results of the pantograph-catenary interaction benchmark. *Veh Syst Dyn* 2015;53:412-35. DOI

28. Zhang M, Xu F. Tuned mass damper for self-excited vibration control: Optimization involving nonlinear aeroelastic effect. *J Wind Eng Ind Aerodyn* 2022;220:104836. DOI

29. Yang J, Song Y, Lu X, Duan F, Liu Z, Chen K. Validation and Analysis on Numerical Response of Super-High-Speed Railway Pantograph-Catenary Interaction Based on Experimental Test. *Shock Vib* 2021;2021:1-13. DOI

30. Zhai W, Wang K, Cai C. Fundamentals of vehicle-track coupled dynamics. *Veh Syst Dyn* 2009;47:1349-76. DOI

31. Ouyang H. Moving-load dynamic problems: A tutorial (with a brief overview). *Mech Syst Signal Process* 2011;25:2039-60. DOI

32. Lopez-Garcia O, Carnicero A, Maroño JL. Influence of stiffness and contact modelling on catenary-pantograph system dynamics. *J Sound Vib* 2007;299:806-21. DOI

33. Ye Y, Huang P, Sun Y, Shi D. MBSNet: A deep learning model for multibody dynamics simulation and its application to a vehicle-track system. *Mech Syst Signal Process* 2021;157:107716. DOI

34. Zhai W. Vehicle-track coupled dynamics models, 3th ed. Beijing: Science Press, 2020. DOI

35. European Committee for Electrotechnical Standardization. EN 50318. Railway applications - current collection systems - validation of

simulation of the dynamic interaction between pantograph and overhead contact line. Brussels: European Standards (EN), 2018.

36. Sorrentino S, Anastasio D, Fasana A, Marchesiello S. Distributed parameter and finite element models for wave propagation in railway contact lines. *J Sound Vib* 2017;410:1-18. DOI

37. Wu TX, Thompson DJ. On the parametric excitation of the wheel/track system. *J Sound Vib* 2004;278:725-47. DOI

38. Ambrósio J, Pombo J, Pereira M. Optimization of high-speed railway pantographs for improving pantograph-catenary contact. *Theor Appl Mech Lett* 2013;3:013006. DOI

39. Pombo J, Ambrósio J. Influence of pantograph suspension characteristics on the contact quality with the catenary for high speed trains. *Comput Struct* 2012;110:32-42. DOI